Journal of South American Earth Sciences 93 (2019) 449–461

Contents lists available at ScienceDirect

Journal of South American Earth Sciences

journal homepage: www.elsevier.com/locate/jsames

Active deformation in Ecuador enlightened by a new waveform-based catalog of earthquake focal mechanisms

Sandro Vaca[a,b,*], Martin Vallée[a], Jean-Mathieu Nocquet[a,c], Alexandra Alvarado[b]

[a] Université de Paris, Institut de physique du globe de Paris, CNRS, F-75005, Paris, France
[b] Instituto Geofísico-Escuela Politécnica Nacional, Quito, Ecuador
[c] Université Côte d'Azur, IRD, CNRS, Observatoire de la Côte d'Azur, Géoazur, Sophia Antipolis, France

A B S T R A C T

The recent development of a national seismic broadband network in Ecuador enables us to determine a comprehensive catalog of earthquake focal mechanisms at the country-scale. Using a waveform inversion technique accounting for the spatially variable seismic velocity structure across the country, we provide location, depth, focal mechanism and seismic moment for 282 earthquakes during the 2009–2015 period. Our results are consistent with source parameter determinations at the global scale for the largest events, and increase the number of waveform-based focal mechanism solutions by a factor of two. Our new catalog provides additional constraints on the active deformation processes in Ecuador. Along the Ecuador margin, we find a correlation between the focal mechanisms and the strength of interseismic locking at the subduction interface derived from GPS measurements: thrust earthquakes predominate in Northern Ecuador where interseismic locking is high, while the low-to-moderate locking in Central and Southern Ecuador results in variable fault plane orientations. Focal mechanisms for crustal earthquakes are consistent with the principal axis of strain rate field derived from GPS data and with the location of the main active faults. Our catalog helps to determine the earthquake type to be expected in each of the seismic zones that have recently been proposed for probabilistic seismic hazard assessment.

1. Introduction

The northern Andes is an area of complex tectonics due to the interaction of the Nazca, South America and Caribbean plates (Pennington, 1981; Kellogg and Bonini, 1982; Ego et al., 1996). The oblique convergence of the oceanic Nazca plate below the South America continent (Fig. 1) is partitioned between westward slip at the subduction interface and a northeastward escape of the North Andean Sliver (NAS) relative to South America (e.g., Pennington, 1981; Kellogg et al., 1985; Freymueller et al., 1993; Audemard and Audemard, 2002; Trenkamp et al., 2002; Nocquet et al., 2014; Mora-Páez et al., 2018, Fig. 1). The NAS motion is predominantly accommodated by a large-scale regional dextral fault-system (Soulas et al., 1991), starting at the southern boundary of the Caribbean plate in Venezuela, running across Colombia along the foothills of the Eastern Cordillera (e.g., Taboada et al., 1998), entering into Ecuador where it crosses the Andean cordillera, before finally reaching the gulf of Guayaquil (e.g., Audemard, 1993; Nocquet et al., 2014; Alvarado et al., 2016; Yepes et al., 2016; Fig. 1). In Ecuador, this major fault system has been named the Chingual-Cosanga-Pallatanga-Puná (CCPP) fault system, in reference to its individual segments (Alvarado et al., 2016). Secondary fault systems, with significant seismic hazard shown by large historical earthquakes (Beauval et al., 2010, 2013), are also found west of this major fault system in the inter-andean valley, and east of it in the sub-andean domain (Alvarado et al., 2014, 2016; Yepes et al., 2016) (Fig. 1).

Along the Ecuadorian margin, elastic strain accumulation is heterogeneous. In northern Ecuador, the high interseismic locking imaged by GPS (Fig. 1) is consistent with the large megathrust earthquakes observed during the XXth century [1906, Mw 8.4–8.8 (Kelleher, 1972; Kanamori and McNally, 1982; Ye et al., 2016; Yoshimoto et al., 2017); 1942, Mw 7.8 (Mendoza and Dewey, 1984); 1958, Mw 7.7 (Swenson and Beck, 1996); 1979, Mw 8.1 (Beck and Ruff, 1984)] and with the recent Mw 7.8 2016 Pedernales earthquake (Ye et al., 2016; Nocquet et al., 2017; Yoshimoto et al., 2017).

Between latitudes 0.8S and 1.5S, the average coupling is low and only a small, shallow area close to La Plata island is found to be locked (Vallée et al., 2013; Chlieh et al., 2014; Collot et al., 2017). South of this area, the GPS data do not detect any significant coupling (Nocquet et al., 2014; Villegas-Lanza et al., 2016).

Aside from the large subduction earthquakes, destructive events mostly occurred along or close to the CCPP (Beauval et al., 2010, 2013; Alvarado et al., 2016; Yepes et al., 2016). Large crustal events are expected to have long recurrence intervals (Baize et al., 2015), and as a consequence, historical events cannot fully characterize the type and locations of potential future earthquakes. An approach complementary to the historical earthquake catalog is to determine the rupture mechanism of small and moderate earthquakes. A preliminary attempt to characterize the seismogenic zones in Ecuador was made by Bonilla

* Corresponding author. Instituto Geofísico-Escuela Politécnica Nacional, Quito, Ecuador.
E-mail address: svaca@igepn.edu.ec (S. Vaca).

https://doi.org/10.1016/j.jsames.2019.05.017
Received 13 June 2018; Received in revised form 10 May 2019; Accepted 10 May 2019
Available online 12 May 2019
0895-9811/

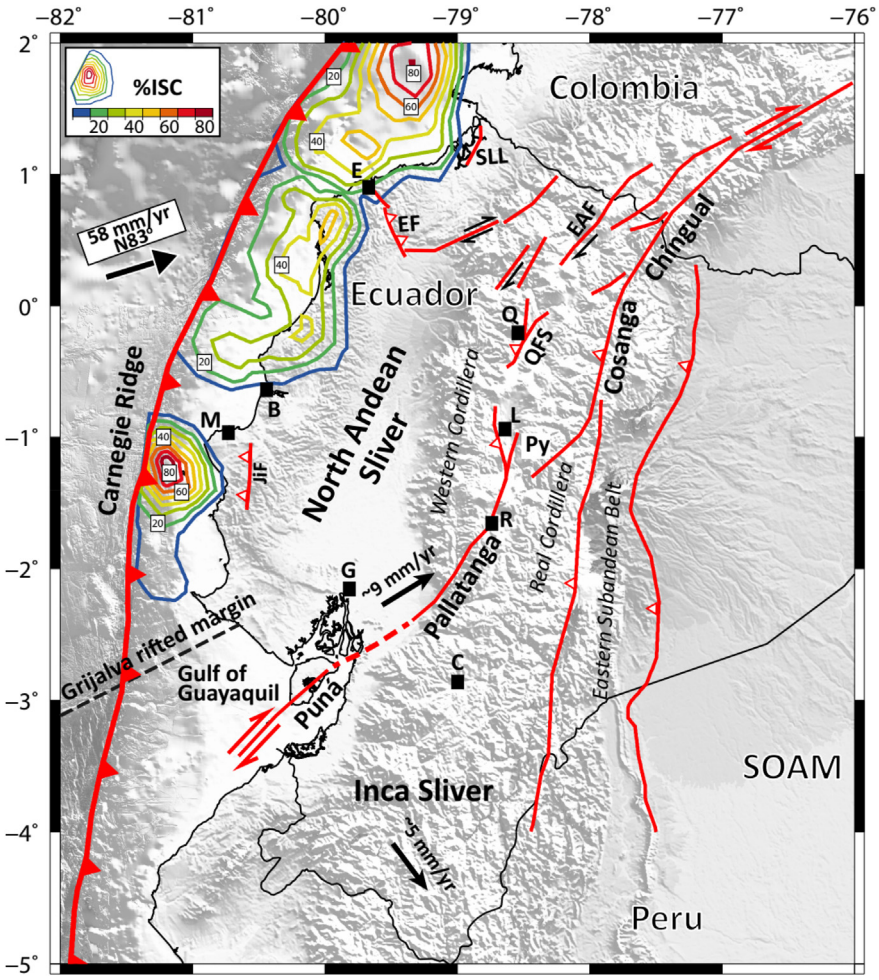

Fig. 1. Tectonic map of Ecuador. The Nazca plate converges obliquely with respect to the stable South American plate (SOAM) at 58 mm/yr (Kendrick et al., 2003), and relatively to the North Andean Sliver (NAS) at 47 mm/yr (Nocquet et al., 2014). The interseismic coupling (ISC) model from Chlieh et al. (2014) is shown by the colored contours. With respect to stable South America, the NAS moves NNE-ward at ~9 mm/yr along the Chingual-Cosanga-Pallatanga-Puná (CCPP) fault system (Nocquet et al., 2014; Alvarado et al., 2016). The Inca Sliver is moving toward the SSE at ~5 mm/yr (Nocquet et al., 2014; Villegas-Lanza et al., 2016), inducing shortening in the eastern sub-Andean belt. The Grijalva fracture separates two domains of the Nazca plate with different ages and densities (Lonsdale, 2005). Faults: SLL: San Lorenzo lineament; EF: Esmeraldas Fault; EAF: El Angel Fault; JiF: Jipijapa Fault; Py: Pisayambo zone; QFS: Quito active Fault System. Cities: E: Esmeraldas; B: Bahía; M: Manta; G: Guayaquil; Q: Quito; L: Latacunga; C: Cuenca; R: Riobamba.

et al. (1992) who determined the spatial distribution of the active fault systems, using the earthquake depths and faulting styles provided by the focal mechanisms solutions. More recently, Yepes et al. (2016) proposed a new classification for the seismic source zones (SSZs) for subduction interface, intraslab and crustal events. Their classification takes into account focal mechanisms from the Global centroid moment tensor (GCMT) catalog (Dziewonski et al., 1981; Ekström et al., 2012), geological and geophysical information (tectonic and structural features of major faults, geodesy and paleoseismology). In total 19 SSZs have been characterized corresponding to the shallow subduction interface (3), intraslab (6), crustal (9), and outer rise (1) zones. Each of the SSZ is assumed to have a homogeneous seismogenic potential (Yepes et al., 2016). In this study, we use the zonation proposed by Yepes et al. (2016) and discuss its relations with our newly determined focal mechanism catalog.

2. Development of the broadband seismic network and new potential for source parameters determination

For the main part of the XXth century, Ecuador has been seismically instrumented only by sensors in the vicinity of its capital Quito. In 1904, the Astronomical Observatory installed there the first seismic instrument (Bosh-Omori), which was then replaced by a Mainka instrument in 1928. Later, a set of Sprengnether seismometers (two horizontal and one vertical components) was deployed in 1954. In 1963, the QUI station (composed of 3 high-gain and 3 long period instruments, both with horizontal and vertical components (López, 2005)) was installed in the western part of Quito in the framework of the World-Wide Standardized Seismographic Network (WWSSN). This station was moved in 1975 to South-west of Quito and was maintained until the 1980's by the “Instituto Geofísico de la Escuela Politécnica Nacional” (IG-EPN).

The local Ecuadorian seismic network started in the 1970's, with short period seismic stations mostly deployed temporarily in order to monitor volcanic activity and specific areas of the Inter-Andean-Valley (Yepes, 1982; Durand et al., 1987). The density of the stations in the Andes improved after the creation of the IG-EPN in 1983, and the seismic network was eventually extended to the coastal areas after 1991 (Vaca, 2006). In 2002, the IRIS GSN station OTAV (close to Otavalo city) was the first permanent broadband station with real time transmission installed in the country. Since 2006, the seismic network has been regularly improved thanks to the efforts of IG-EPN together with the support of national government agencies (SENESCYT and SENPLADES), national and international partners (local governments, IRD, JICA, USAID, see Alvarado et al., 2018). The densification of the broad band network in the north-western zone of Ecuador started at the end of 2008 with the ADN-project (Nocquet et al., 2010). Since 2011, a country-scale broadband network is progressively being installed, with the final objective to cover the most seismically active regions, from the coastal zone to the eastern foothills with an average ~50 km inter-station distance (Fig. 2).

Among other applications, the development of a country-wide broadband seismic network now allows us to determine the earthquake source parameters by waveform modeling. Since 2009, most of the events with moment magnitudes Mw > 3.5 could be analyzed with the method described in the next section. Even with only a few years of data, a significant information increase is expected compared to the GCMT catalog, which has a magnitude threshold of about Mw 5.0. We

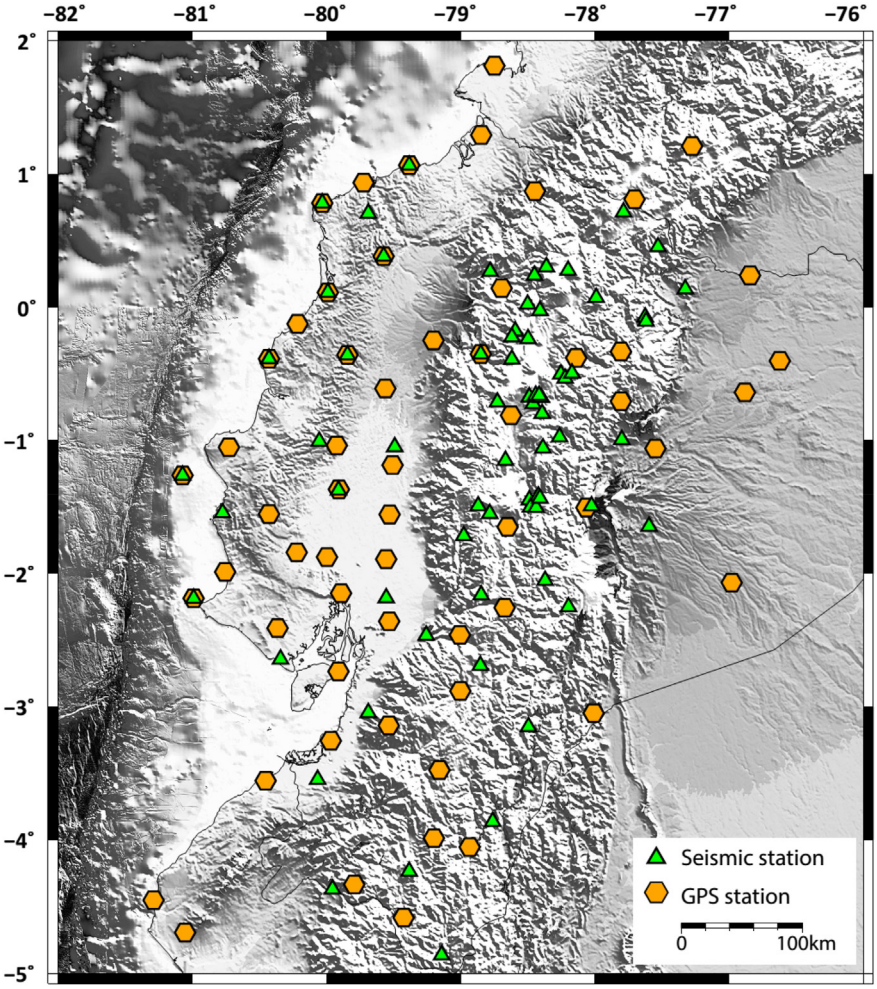

Fig. 2. Seismic (broadband, green triangles) and GPS networks (orange hexagons, Mothes et al., 2013, 2018; Alvarado et al., 2018) in Ecuador as of December 2015. The dense arrays of seismic stations in the central-northern part of the country are used for volcano monitoring. Additional GPS stations in northern Peru and southern Colombia helping to define the regional kinematics are also shown. (For interpretation of the references to color in this figure legend, the reader is referred to the Web version of this article.)

also expect to improve the focal mechanism information previously provided by IG-EPN, which was based on first arrival polarities. Our final objective is to contribute to the "Ecuadorian focal mechanism catalog", in which we will also provide more reliable information about source depths and moment magnitudes.

3. Focal mechanism, depth and magnitude determination

Several similar methods exist to analyze the broadband seismic waveforms in order to retrieve the source parameters [e.g. FMNEAR (Delouis, 2014); ISOLA (Zahradník et al., 2008)]. Here, we use the MECAVEL method, already used in several studies of moderate magnitude earthquakes (Mercier de Lépinay et al., 2011; Grandin et al., 2017). A specificity of the MECAVEL method is its ability to solve for the velocity model simultaneously with the searched source parameters (strike, dip, and rake of the focal mechanism, centroid location, source origin time and duration, and moment magnitude). The method starts from an initial solution (for origin time, hypocenter, and magnitude), here determined by IG-EPN. The velocity model is parametrized by a superficial low-velocity layer above a crustal structure with variable Moho depth. Crustal velocities are searched over a wide range, between 5.5 km/s and 6.7 km/s, and Moho depth can reach up to 67 km. This approach is particularly useful when analyzing earthquakes occurring in different tectonic environments, as it is the case in Ecuador. Modeled waveforms in the tabular velocity model are computed using the discrete wave number method from Bouchon (1981), and the inverse problem is solved through the Neighborhood Algorithm (Sambridge, 1999). Within the MECAVEL method, the three-component displacement waveforms are bandpassed between a low frequency (F_{c1}) and a high frequency (F_{c2}) threshold. F_{c1} is typically chosen above the low-frequency noise that may affect the waveforms for a moderate earthquake and F_{c2} is mostly controlled by the limited accuracy of the simplified one-dimensional structure model. F_{c2} must also not be chosen above the earthquake corner frequency, because the earthquake time history is simply modeled by a triangular source time function whose only inverted parameter is the global duration. In most of the cases analyzed here, F_{c1} on the order of 0.02–0.04 Hz and F_{c2} on the order of 0.05–0.07 Hz are found to be suitable values. As a consequence, the source duration has a real role in the inversion procedure only for large events (Mw $>$ 6.5), for which it affects frequencies close to F_{c2}.

We extract all events reported with local magnitude larger than 3.8 from the Ecuadorian national earthquake catalog (IG-EPN) for the period 2009–2015, and collect all the available broadband seismic data in Ecuador. We then manually select the most suitable waveforms, taking into account distance and azimuthal coverage and eliminating components with a poor signal-to-noise ratio. For the 544 events with magnitude above 3.8, 326 were recorded with a quality sufficient for the waveform analysis.

We use a criterion based on the misfit between data and synthetics, azimuthal coverage, and number of available stations and components,

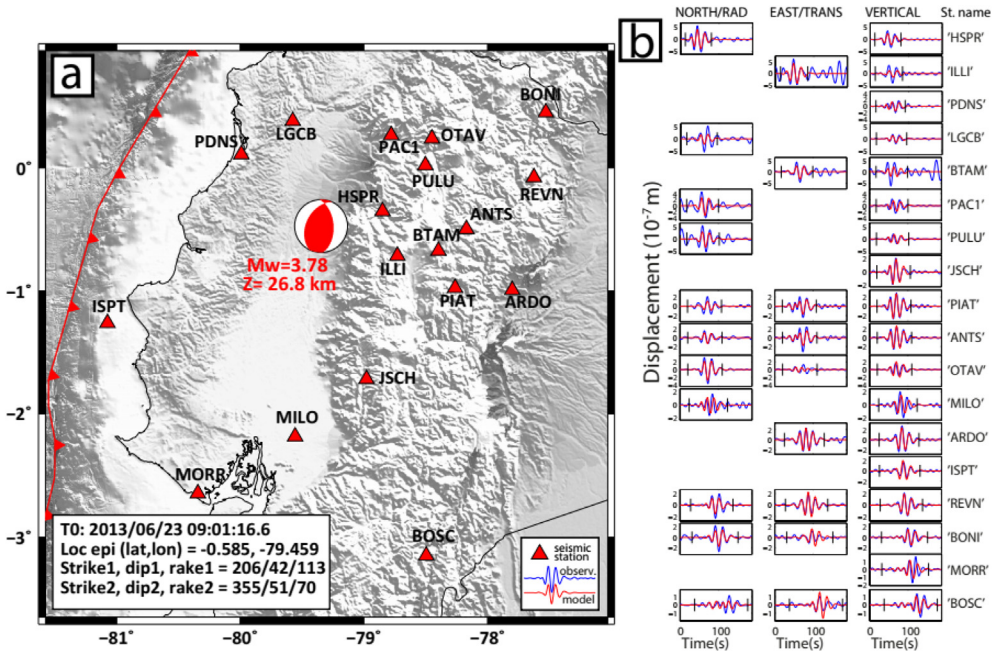

Fig. 3. Example of a solution determined by the MECAVEL method. The map in (a) shows the inverted source parameters (focal mechanism, moment magnitude Mw and depth Z) and the location of the broadband seismic stations used. The red line represents the trench. The left-bottom inset provides the origin time (T0), the epicentral location and the angles (strike, dip, and rake) of the two conjugate focal plane solutions. The agreement between observed (blue) and synthetic (red) waveforms is shown in b) for each station and component. The stations are sorted by increasing epicentral distance from top to bottom. Here, data and synthetics are filtered between 0.04 Hz and 0.06 Hz. We excluded some components because of their poor signal-to-noise ratio in the selected frequency range. (For interpretation of the references to color in this figure legend, the reader is referred to the Web version of this article.)

in order to ensure that only reliable solutions are kept. 44 events not meeting these criteria were rejected, resulting in a final catalog of 282 events. This catalog is provided as a public dataset linked to the present study (Vaca et al., 2019). Rejections are mostly related to earthquakes with low magnitudes located far away from the seismic network, and/or to earthquakes with an erroneous initial location preventing the MECAVEL method to converge. An example of focal mechanism determination for a Mw 3.8 earthquake is shown in Fig. 3.

As a first validation of our method, we compared our results to the Global CMT solutions for the 34 events found in common during the 2009–2015 period. These earthquakes have a magnitude between Mw 4.8 and Mw 7.1 (Figs. 4–6). The focal mechanisms are very similar in almost all cases, even when compared to the full GCMT solution which includes the non-double-couple components. Only one event (2014/10/20, marked with a black asterisk in Fig. 4) located in the Andes close to the Ecuador-Colombia border, is significantly different. This event occurred during a seismic crisis related to a magmatic intrusion in the Chiles-Cerro Negro volcanic complex (IG-EPN, OSVP internal reports, Ebmeier et al., 2016). In such a context, a complex mechanism reflecting the superposition of volumetric changes and shear faulting (McNutt, 2005; Minson et al., 2007; Shuler and Ekström, 2009) would explain the strong non-double-couple component of the GCMT-solution and the difficulty to resolve this event with the double-couple MECAVEL method.

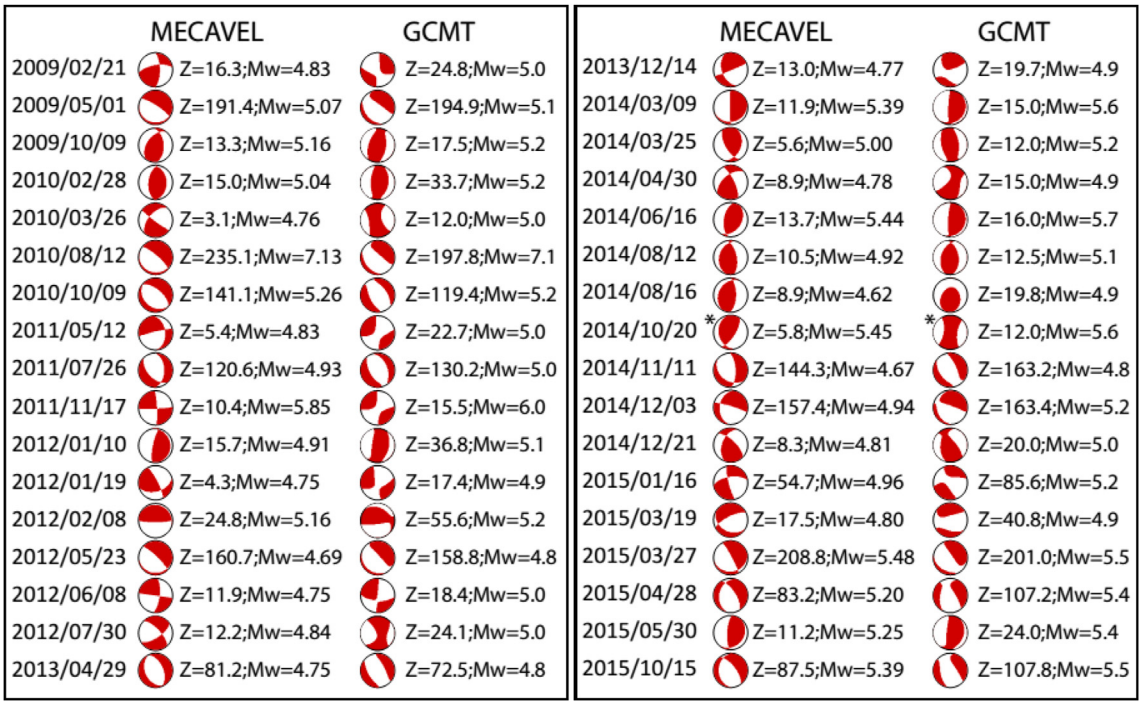

Fig. 4. Comparison between MECAVEL (double couple) with GCMT solutions (full solution) for the common events of the 2009–2015 period. The date of the earthquake occurrence is shown to the left of the focal mechanisms. Depths (Z) and magnitudes (Mw) are shown to the right of the focal mechanisms.

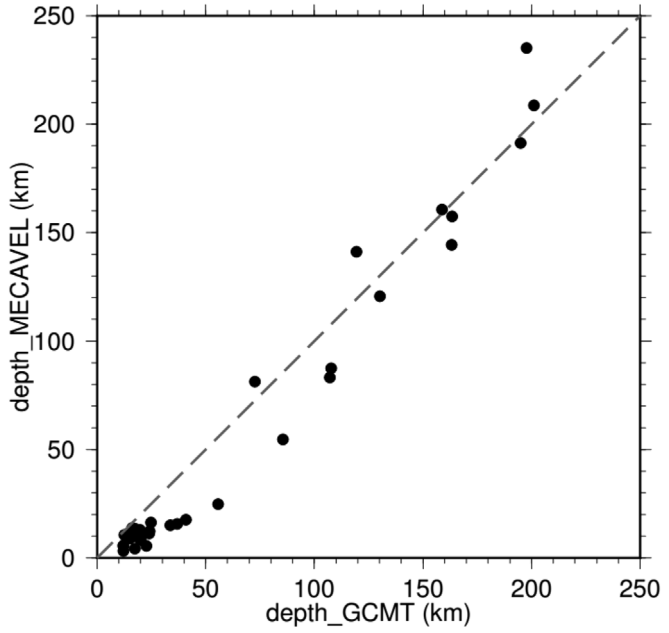

Fig. 5. Depth comparison for the events common to GCMT and MECAVEL (this study). Dashed lines show the line along which the considered depths are equal.

Compared with GCMT results, no general bias is observed for the full depth range, down to 200 km depth, and the average difference is 8 km (Fig. 5). This difference is due to the numerous events with depths shallower than 50 km, for which GCMT determines deeper values than MECAVEL. This trend is likely due both to the minimum allowed depth in the inversion (12 km for GCMT and 3 km for MECAVEL) and to slower velocity structures found by MECAVEL. The comparison of magnitudes shows that those determined with the MECAVEL method are slightly lower than the GCMT ones (average difference of 0.13, Fig. 6). On the contrary, magnitudes from IG-EPN catalog are systematically larger (average difference of 0.38). Such observation should help to homogenize the magnitudes of the local IG-EPN catalog, a step required to use a magnitude catalog for seismic hazard estimation (e.g. Beauval et al., 2013).

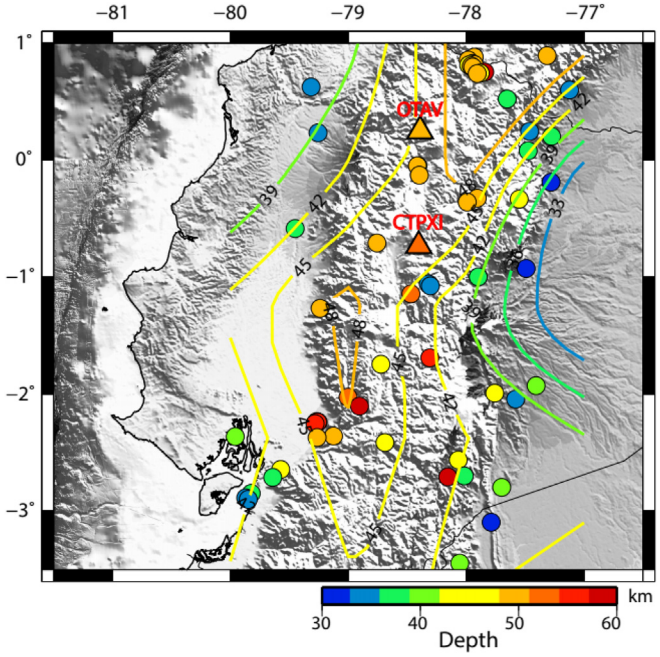

Fig. 7. Moho depths inferred from the MECAVEL inversion results. The depth contours are interpolated from the Moho depths individually determined for each earthquake (colored points). The subduction area is not considered here, as the tabular model is not expected to provide meaningful information in a context of 2D/3D structure complexities. Colored triangles show Moho depths obtained from Receiver Functions at the two following locations: CTPXI (Cotopaxi Volcano) and OTAV (IRIS GSN station close to Otavalo).

As another validation of the MECAVEL method, we show in Fig. 7 that the optimized 1D model is consistent with the large-scale features of the crustal thickness in Ecuador. In particular, the Moho depth approaches 50 km beneath the ~150 km-wide Andes mountain range (Robalino, 1977; Chambat, 1996); and as expected, the crustal thickness is thinner when entering into the subandean area or into the coastal domain. Crustal thicknesses obtained from Receiver Functions show Moho depths of ~53 km under the Cotopaxi volcano in the central Andes (Bishop et al., 2017), and of ~50 km below OTAV station

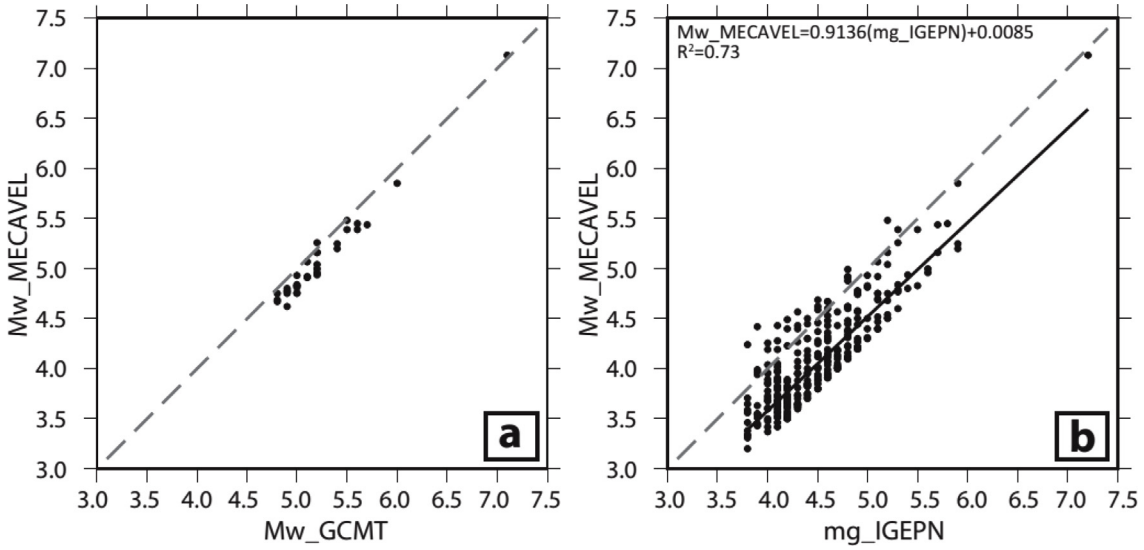

Fig. 6. Magnitude comparison for the events common to GCMT, MECAVEL (this study) and IG-EPN local catalog. a) Comparison between GCMT and MECAVEL b) Comparison between MECAVEL and IG-EPN. In b) we show the equation of the linear regression (thick line) between the two magnitude catalogs (and the associated correlation coefficient R^2). This equation can be used to convert the local magnitudes to moment magnitudes in order to homogenize the local catalog. In a) and b) the dashed lines show the line along which the considered magnitudes are equal. "mg_IGEPN" refers to the preferred magnitude reported by IG-EPN.

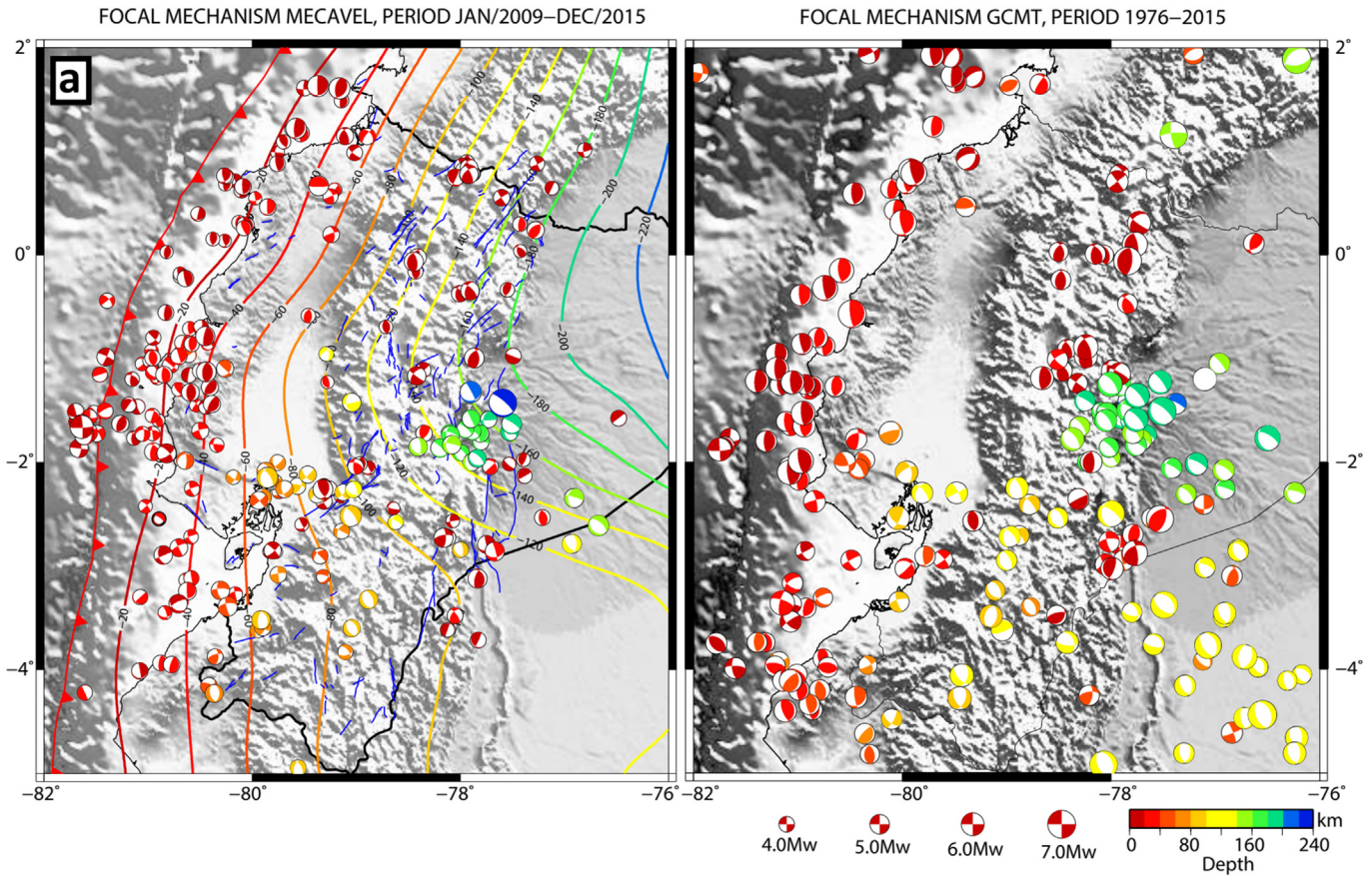

Fig. 8. Focal mechanisms provided (a) by the MECAVEL method (this study, 2009–2015) and (b) by the GCMT double-couple solutions (1976–2015). In a) and b) the earthquake depths and the iso-depths (in km) contours of the slab (Hayes et al., 2012) are color-coded with the same color scale (shown at the bottom right). The thick red line with triangles represents the trench. (For interpretation of the references to color in this figure legend, the reader is referred to the Web version of this article.)

(Poveda et al., 2015). We show in Fig. 7 that the latter values are consistent with the neighboring Moho depths inferred from MECAVEL. Crustal depths determined in the subduction area (not shown in Fig. 7) are less consistent from one earthquake to the other, which can be simply understood by the fact that the one-dimensional parametrization is too simplistic in a subduction context. This generally illustrates that in a structurally complex area, the velocity structure determined by the MECAVEL method has to be considered as an equivalent model, possibly not directly related to the actual structure.

In Fig. 8, we finally show the 210 solutions reported by GCMT (Ekström et al., 2012) for the 1976–2015 period together with the 282 solutions determined here in the 2009–2015 period. We observe a general consistency of the focal mechanisms between the two catalogs, in all of the seismically active areas of the country. The two catalogs complement each other, with areas where information about the earthquake mechanism type is richer in the MECAVEL or, on the contrary, in the GCMT catalog. In the next section, we discuss the combined catalog in the light of the active deformation processes in Ecuador. This combined catalog uses the MECAVEL solution for the events common with GCMT, but as shown by the similarities of the 34 common solutions in Fig. 4, this choice does not influence any further interpretation of the focal mechanisms.

4. Focal mechanisms and deformation processes in Ecuador

For the sake of clarity, we separate the focal mechanism (FMs) according to their depths and their locations along the margin or in the continental domain. Figs. 9 and 10 show events shallower than 35 km (used to analyze the partitioning features in Fig. 11), and Fig. 12 shows the events deeper than 35 km. Although this division is somehow arbitrary, it is convenient to first discuss the state of stress at the subduction interface and within the overriding plate. Within the continental domain, it allows to separate the events related to crustal tectonics from deep slab-related events.

4.1. Subduction

Overall, the location of the earthquakes studied here is in agreement with the study from Font et al. (2013), who found that earthquakes during the interseismic period are spatially organized into several stripes of seismicity, most of them being perpendicular to the trench (Fig. 9).

4.1.1. Northern Ecuador

This zone hosted a large megathrust earthquakes sequence during the XXth century with magnitudes Mw 7.7–8.8 (Kelleher, 1972; Beck and Ruff, 1984; Mendoza and Dewey, 1984; Swenson and Beck, 1996). In our catalog, this area is characterized by thrust events at or close to the subduction interface (Fig. 9). An interesting spatial correlation shows up with the interseismic locking models. Indeed, from latitude 0.8°N and further north, high locking is found from the trench to a depth of ~30 km. Location of the focal mechanisms determined here appears to outline the area of high locking, with only very few events located within areas of locking higher than 60% (Fig. 9). Focal mechanisms rather correlate with areas of the largest interseismic locking gradients, either downdip or laterally. This observation is for instance similar to the Himalaya where the small seismicity appears to delimit the downdip limit of locking, where shear stress at the interface is the

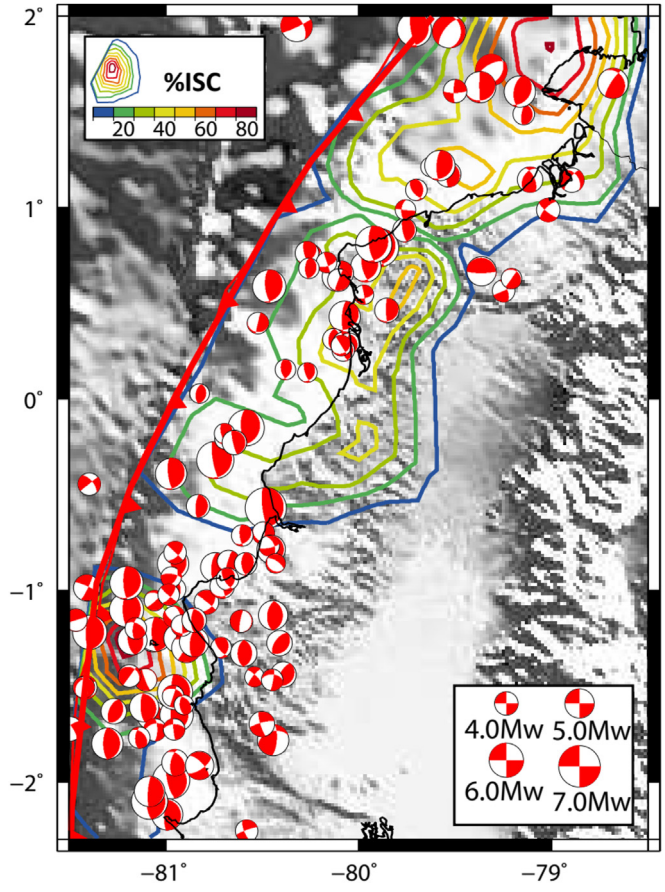

Fig. 9. Combined GCMT and MECAVEL (1976–2015) shallow FMs solutions (depth shallower than 35 km) for the central and northern Ecuador margin. The interseismic locking model from Chlieh et al. (2014) is shown by the colored contours. The thick red line with triangles represents the trench. (For interpretation of the references to color in this figure legend, the reader is referred to the Web version of this article.)

largest during the interseismic period (Avouac et al., 2015). This seismicity also appears to occur during seismic swarms related to slow slip events as found by Vaca et al. (2018) for the Punta-Galera Mompiche zone area located around lat. 0.8°N. The thrust mechanisms found in this study are compatible with this interpretation, although a few shallow strike-slip mechanisms reflect additional deformation within the overriding plate along the San Lorenzo lineament and the Esmeraldas fault (Fig. 1).

4.1.2. The Pedernales segment

The Pedernales segment, between lat. 0.7°N and 0.5°S, possibly ruptured during the 1906 earthquake, and hosted the 1942 Mw 7.8–7.9 and the recent 2016 Pedernales Mw 7.8 earthquakes (Swenson and Beck, 1996; Ye et al., 2016; Nocquet et al., 2017). Along this segment, interseismic locking is confined between 10 and 30 km depth, in agreement with the location of the 2016 Pedernales earthquake, whose main rupture propagated below the coast between latitudes 0.4°N and 0.4°S (Nocquet et al., 2017). Our catalog, which ends in 2015, exhibits interesting spatial relationships with the rupture areas of the forthcoming Pedernales earthquake. First, our catalog shows that very few earthquakes occurred within the area of large (> 1 m) co-seismic slip of the Pedernales earthquake (Fig. 9 and Nocquet et al., 2017) during the years before the event. Secondly, at lat. ~0.2°S, our catalog highlights a larger density of events. That area did not rupture during the 2016 earthquake but experienced large and rapid localized afterslip immediately after (Rolandone et al., 2018). It also hosted regular seismic swarms (Segovia, 2016) and repeating earthquakes during the years before the Pedernales earthquakes, although no associated slow slip event here has been geodetically found yet (Rolandone et al., 2018). The focal mechanisms found in this study are also predominantly thrust, consistent with slip at the interface (Figs. 9 and 10). In that area, deformation therefore does not appear to be accommodated by infrequent large earthquakes, but rather by numerous moderate earthquakes, seismic swarms (possibly associated with aseismic slip) and afterslip.

4.1.3. The Bahía de Caráquez and La Plata Island segments

The Bahía area (Figs. 9 and 10), between latitudes 0.5°S and 1°S, experienced three M ~7 earthquakes in 1896, 1956 and 1998 (Mw 7.1) (Segovia et al., 1999; Yepes et al., 2016). In that area, our study shows mostly thrust mechanisms, compatible with interface subduction earthquakes. Although Yepes et al. (2016) consider the Pedernales and Bahía asperities to behave independently one from each other, the seismicity distribution does not show clear patterns to support this view. The Bahía and Pedernales segments are now considered as the same seismic zone (Beauval et al., 2018).

Between latitudes 1°S and 1.5°S, the central margin in Ecuador includes a 50 × 50 km^2 area of high ISC (Figs. 1 and 9), around the "La Plata Island", found to correlate with the presence of a subducted oceanic relief (Collot et al., 2017). This zone marks a transition between the mostly locked areas to the north and the southern Talara zone (Fig. 10) which shows weak to negligible interplate locking. Episodic slow slip events, associated with seismic swarms seem to release part of the slip deficit there (Vaca et al., 2009; Font et al., 2013; Vallée et al., 2013; Chlieh et al., 2014; Jarrin, 2015; Segovia et al., 2018). In the central margin, the mechanisms of the abundant seismicity are more diverse than in Northern Ecuador (Figs. 9 and 10), varying from reverse to strike-slip. The presence of Carnegie ridge may be an element explaining this variability, perhaps through the influence of various seamounts locally perturbing the stress field (Collot et al., 2017). Alternatively, strike-slip events might be located within the slab, indicating internal deformation of the subducting Carnegie ridge.

This area also shows outer-rise seismicity occurring within the Nazca plate, west of the trench, in the Carnegie ridge domain (Figs. 9 and 10). Part of the seismicity might be related to the slab flexure (Collot et al., 2009), which is evidenced here by the presence of a few normal mechanisms. Nevertheless, most of the earthquakes show strike-slip mechanisms with planes azimuths ranging from N–S to NE-SW, like the one of 2011/11/17 (Mw 5.9 MECAVEL, Mw 6.0 GCMT; Figs. 4 and 8–10). Such kind of seismicity could be related to two aligned ridges of ~W-E direction (with a 30 km separation) and to some structures of the Nazca Plate aligned N55°E, observed in the bathymetry (Michaud et al., 2006; Collot et al., 2009). Because of the recurrent seismicity and the reported magnitudes, we suggest that the outer-rise Carnegie ridge could be added as an additional seismic zone for future PSHA models.

Further inland, an aligned N–S cluster with mostly reverse FMs is observed between lat. 1.8°S and 1.2°S. Béthoux et al. (2011), observing a similar pattern of focal mechanisms, suggest that some of them are not related to the interface but to the N–S oriented Jipijapa fault (Fig. 1) (Egüez et al., 2003), especially those showing steep dips (~30°) and shallow hypocenters (less than 20 km depth).

4.1.4. Southern Ecuador and northern Peru

South of the Grijalva fracture (Fig. 10), very few thrust events are observed. This can be related to the very low subduction interface locking in this area (Nocquet et al., 2014; Villegas-Lanza et al., 2016). The faulting mechanisms are dominantly strike-slip with a few normal events (Fig. 10), in agreement with the NNE-SSW opening of the Gulf of Guayaquil (Deniaud et al., 1999; Calahorrano, 2005; Witt et al., 2006) and the relative motion between the NAS and the Inca Sliver (Nocquet et al., 2014).

Interestingly, we observe a general correlation between the level of locking and the diversity of focal mechanisms. For the locked Northern

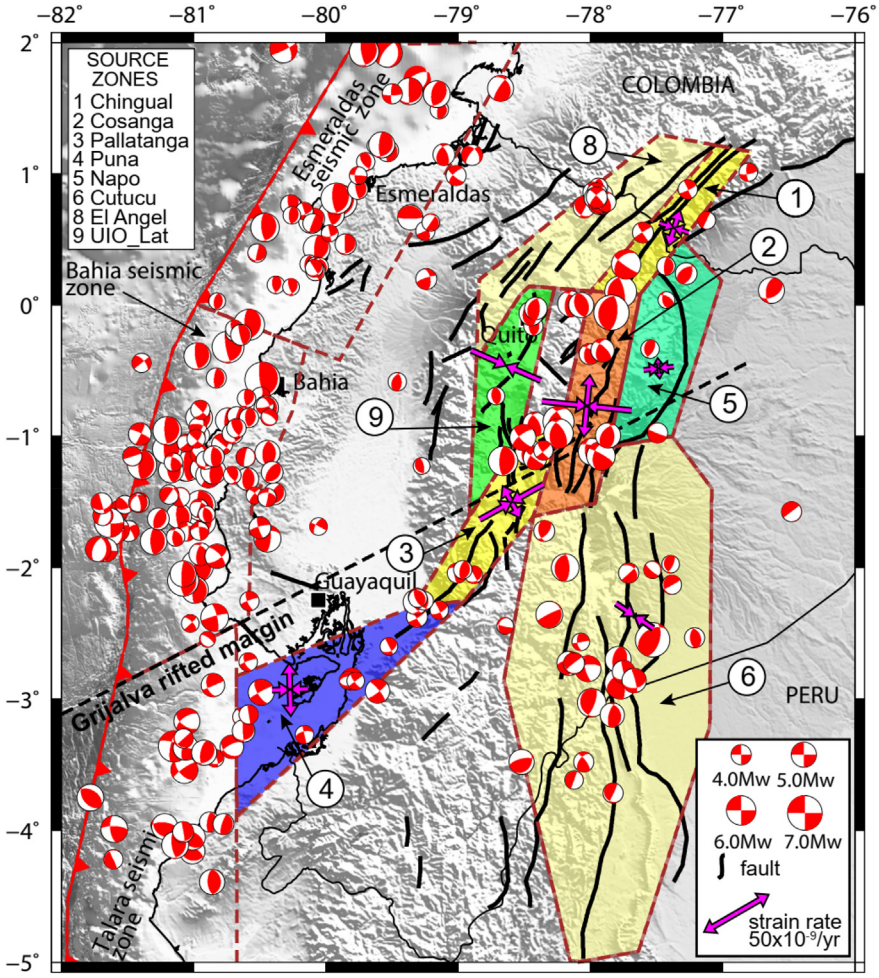

Fig. 10. Joint CGMT and MECAVEL shallow FM solutions (depth shallower than 35 km). We keep the conventions chosen by Yepes et al. (2016) for interface (non-colored polygons) and upper-crustal (colored polygons) seismic source zones (SSZs). Faults distribution is modified from Alvarado et al. (2016). The strain rate axes are calculated from GPS velocities measured within or close from each SSZ (see Fig. S1 and Table S1). We exclude the strain tensor of El Angel SSZ, because too few velocities are available there. The red line represents the trench. (For interpretation of the references to color in this figure legend, the reader is referred to the Web version of this article.)

segments (see Fig. 1), thrust mechanisms consistent with the Nazca-NAS convergence dominate, suggesting that locking at the plate interface controls the stress field both at the plate interface and within the overriding margin. Oppositely, south of La Plata Island (~1.5°S) where locking is weak or confined to the shallowest part of the subduction interface, thrust mechanisms show variable orientations of shortening. Additionally, normal and strike-slip mechanisms, consistent with known crustal faults (e.g. Béthoux et al., 2011) are frequent. Thus, the

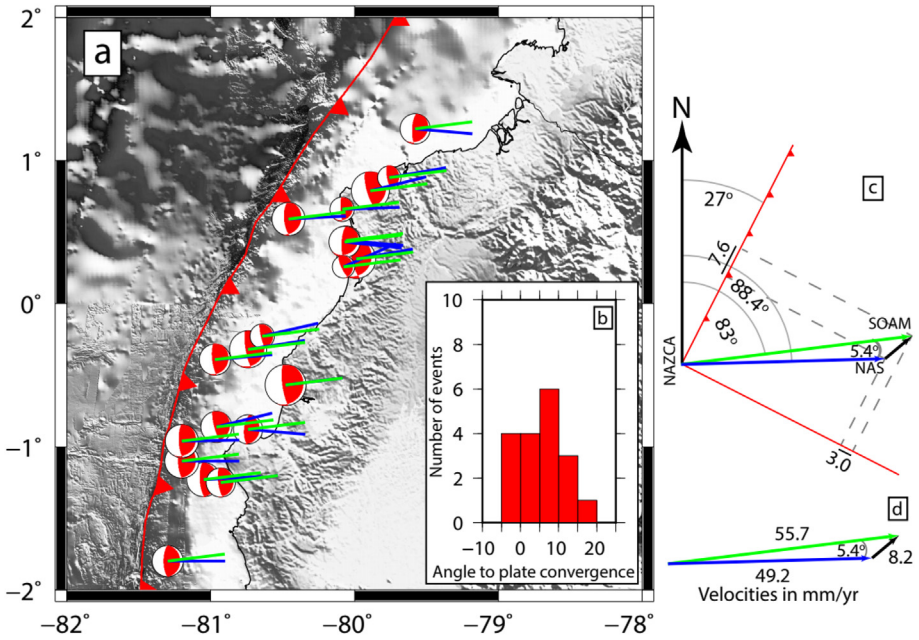

Fig. 11. Partitioning indicated by FMs (GCMT and MECAVEL) subduction interface events. (a) The surface-projected slip vector of each focal mechanism is shown by blue lines, together with the Nazca/SOAM convergence direction (green lines). (b) The histogram shows the angle (in degrees) between Nazca/SOAM convergence direction and slip vector direction, by bins of 5°. Values range between −5° and 15°, resulting in an average and standard error of 5.4° and 6.2°, respectively. (c) Construction of the kinematic triangle. Average azimuth of the trench and its normal (red lines), Nazca/SOAM convergence direction and amplitude (green vector), and the mean slip direction deduced from FMs (blue) are first reported. The additional information on the NAS/SOAM relative direction (black arrow, ~50° azimuth), constrained by the purely strike-slip motion observed in the Chingual area (zone 1 in Fig. 10), allows us to determine the kinematic triangle. This kinematic triangle is shown in (d) with the assumed velocity of Nazca/SOAM (green), and the computed velocities of Nazca/NAS (blue) and NAS/SOAM (black). (For interpretation of the references to color in this figure legend, the reader is referred to the Web version of this article.)

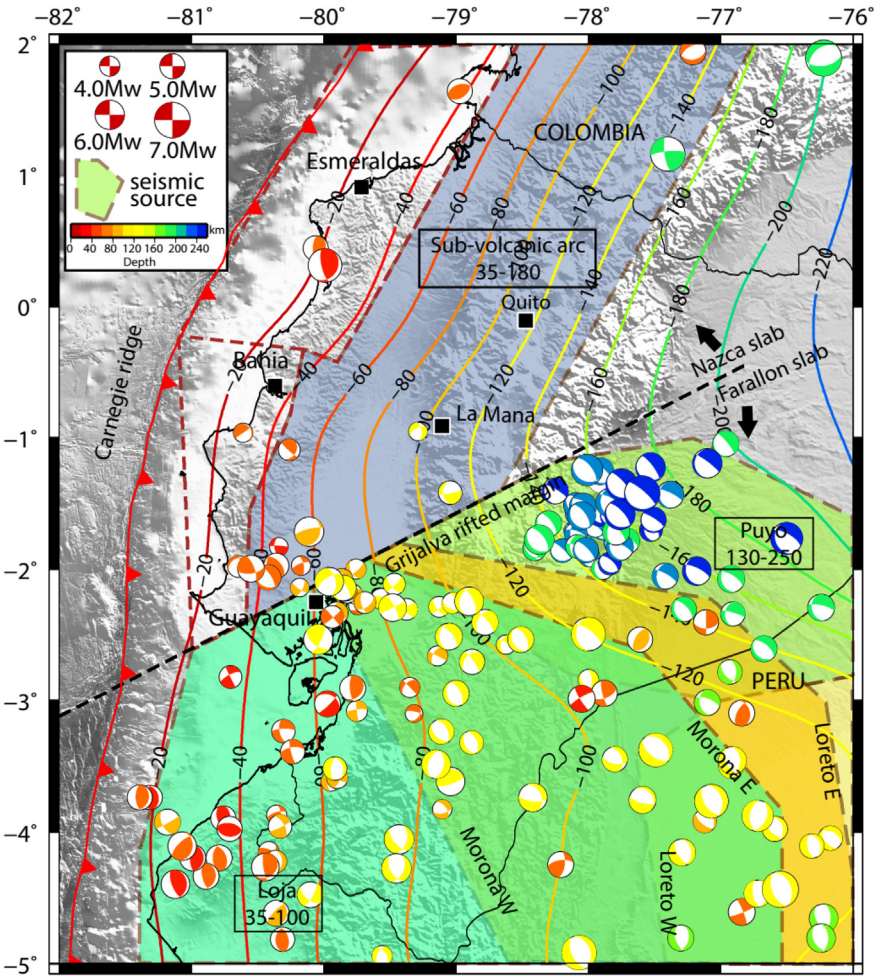

Fig. 12. Joint CGMT and MECAVEL deep focal mechanisms (depth larger than 35 km). We follow the denomination chosen by Yepes et al. (2016) for the name of the seismic sources zones and related features. The Grijalva rifted margin (black dashed line) is believed to have a relevant role because it separates two different slab domains with very different seismic activities (Yepes et al., 2016). The focal mechanism depths and the iso-depths contours of the slab (Hayes et al., 2012) are color-coded with the same scale, shown in the legend. The red thick line represents the trench. (For interpretation of the references to color in this figure legend, the reader is referred to the Web version of this article.)

heterogeneous stress field along that segment therefore appears to result from a combination of crustal stress associated with slow straining of the overriding plate and reduced compressional stress in the plate convergence direction.

4.1.5. Strain partitioning in the Ecuadorian subduction regime

In subduction contexts with oblique convergence, the motion obliquity is generally not fully accommodated by slip at the plate interface (e.g. McCaffrey, 1992). In this case, a forearc sliver is expected to move in a direction parallel to the trench, resulting in strike-slip faulting along one or several faults within the overriding plate (e.g., Chemenda et al., 2000). In addition, the trench perpendicular component of plate convergence may also be partitioned between slip at the subduction interface and thrust in the back-arc domain.

We examine here how focal mechanisms observed in Ecuador help to constrain the degree of partitioning. To do so, we first compute the angle difference between the surface-projected slip vector of interplate earthquakes and the Nazca/South America convergence direction. This approach neglects the small 3D component of the slip vector, and relies on the assumption that motion at the subduction interface is fully characterized by earthquakes (even if it can also be accommodated by aseismic processes). We select the FMs (GCMT and MECAVEL) of events located at the margin with hypocentral depths less than 35 km, nodal planes with strikes between 0° and 45°, dip shallower than 25°, and rakes between 90° and 150°, as these events are expected to have sources along the interface (Fig. 11a). After averaging over the earthquakes (Fig. 11 b), the angle difference between the slip vector and the Nazca/South America convergence direction is found equal to 5.4° (± 6.2°), clockwise with respect to the Nazca/SOAM convergence (Fig. 11c and d). Although marginally significant, the average direction of subduction slip vector suggests that the subduction obliquity is not fully accommodated by slip at the subduction interface. Its value is further consistent with the escape of the NAS with respect to SOAM.

To further quantify the amount of partitioning, we use the seismicity observed in the Chingual area (zone 1 in Fig. 10), where most of the FMs are purely strike-slip with one of their nodal planes directed along a ~50° azimuth. Using this additional information together with the amplitude of the Nazca/SOAM convergence (55.7 mm/yr as reported at 0°N by Kendrick et al. (2003)) allows us to determine the kinematic triangle (Fig. 11c and d). The relative motion Nazca/NAS is found equal to 49.2 mm/yr, to be compared with the value of 47.5 mm found by Nocquet et al. (2014). The relative motion NAS/SOAM is found equal to 8.2 mm/y, in agreement with the geological slip rates of 7.3 ± 2.7 mm/yr (Ego et al., 1996; Tibaldi et al., 2007) and the values between 7.5 and 9.5 mm/yr derived from GPS data (Nocquet et al., 2014). If using an average azimuth of 27° for the trench in Northern Ecuador, the ratio of partitioning is about 25% for the along-trench component of the Nazca/South America convergence (Fig. 11c). Normal trench convergence is also partitioned with 6% of the convergence being transferred to the motion of the NAS.

4.2. Crustal deformation

Using the selection of focal mechanisms shown in Fig. 10, we compare the style of faulting with recent kinematic models for inland Ecuador (Alvarado et al., 2016) and the seismic zonation proposed by Yepes et al. (2016). We further compare the principal axes of the horizontal strain rate tensor against the focal mechanisms. The strain rate

tensors provided in Table S1 (Supplemental Information) are derived from the GPS velocities shown in Fig. S1, using least-squares and estimating a constant velocity gradient (Aktug et al., 2009) within the individual areas shown in Fig. 10.

4.2.1. The Chingual-Cosanga-Pallatanga-Puná fault system (CCPP)

The CCPP is the main fault system accommodating the 7.5–9.5 mm/yr motion of the NAS with respect to the stable part of the South America plate (Nocquet et al., 2014; Alvarado et al., 2016). Variation in strike, slip rate and faulting styles have been used to define separated segments for the seismic zonation presented in Yepes et al. (2016).

The Chingual seismic zone is the northern segment of CCPP (Fig. 1, marked as zone 1 in Fig. 10), crossing the border with Colombia. It delimits the boundary between the NAS and the Amazon basin, which is assumed to be part of the stable part of the South America plate, as indicated by small GPS velocity residuals (< 2 mm/yr) east of the Andes. As a consequence, the motion is expected to be mostly right-lateral strike-slip (Ego et al., 1995; Tibaldi et al., 2007). Little seismicity is observed along this segment. The two focal mechanism solutions (see zone 1 in Fig. 10) are consistent with dextral strike-slip on the NE-oriented planes. Nonetheless, the faults located at the feet of the eastern Andes indicate shallow dipping thrust. The strain rate tensor derived from GPS is in good agreement with right-lateral shear along N30° trending faults.

South of the Chingual segment, the Cosanga fault system (zone 2, Fig. 10) delimits the boundary between the NAS and the Sub-andean domain. Focal mechanisms show reverse slip with a slight right-lateral strike-slip component along the NS nodal plane. This seismic source is described as a transpressive zone (Ego et al., 1996; Alvarado et al., 2016; Yepes et al., 2016). Two destructive earthquakes (Mw ~7.0), in the last 60 years (1955 and 1987) (Hall, 2000; Yepes et al., 2016), occurred along the northern portion of this segment. Focal mechanism for the 1987, Mw 7.0 (mainshock) and Mw 5.8 (aftershock) show thrust and strike-slip respectively (Kawakatsu and Proaño, 1991). The strain rate tensor is also in agreement with a right-lateral transpressive regime for this segment.

The Pallatanga seismic source (zone 3) includes the Pallatanga fault itself and the continuously active Pisayambo seismic nest (Aguilar et al., 1996; Troncoso, 2008). The fault cuts diagonally the Inter-Andean-Valley across the Riobamba basin where it seems to divide into several segments (Baize et al., 2015). In its southwestern part, the Pallatanga fault is a right-lateral strike-slip fault (Winter et al., 1993), for which a 1300-3000 year-long recurrence time of Mw ~7.5 earthquakes has been reported from a paleo-seismology study (Baize et al., 2015). The last earthquake occurred in 1797 and generated the highest intensities [magnitude 7.6 derived from intensities, XI MKS] reported in Ecuador (Egred, 2000; Beauval et al., 2010). Focal mechanisms of small magnitude earthquakes show a combination of right-lateral and thrust motions. The northern part of the Pallatanga fault system (Pisayambo) shows highly recurrent seismicity (Segovia and Alvarado, 2009). In this area, the analysis of an Mw 5.0 earthquake in 2010, combining InSAR, seismic and field observations, evidences a steeply dipping fault plane (> 50°) with right lateral displacement (Champenois et al., 2017). Compressional behavior with right-lateral component is indicated by the GPS derived strain rate tensor.

The southernmost segment of CCPP, the Puná seismic source (zone 4) is described as a strike-slip structure, based on geomorphic observations in the Puná Island (Dumont et al., 2005). Dumont et al. (2005) calculated a Holocene slip rate of 5.8–8 mm/yr which is consistent with the relative motion between the NAS and Inca Sliver (Nocquet et al., 2014). No large historical earthquakes have been reported for this segment. The FMs show dextral mechanisms on NE oriented planes, which are consistent with the expected fault direction and the predominant dextral components derived from the strain rate (Fig. 10). A small group of events including a Mw 5.0 earthquake at the foot of the western Andes shows reverse motion with ~EW shortening. This area behaves like a restraining bend linked to non-coplanar segments of the CCPP fault system, similarly to the New Madrid seismic zone (Marshak et al., 2003). In the Gulf of Guayaquil, the diversity of FMs solutions are the result of the complex tectonic environment. Strike-slip motion can be interpreted as a result of activity in a transpressional structures like those observed in Puná Island (Deniaud et al., 1999; Fig. 10). The normal mechanism solutions are related to the drift of NAS, which induces a N–S tensional regime (Witt et al., 2006).

4.2.2. The subandean domain

The Quaternary tectonics of the northern sub-Andean is not well known. The scarce seismicity and the lack of instrumentation, before 2009 (Alvarado et al., 2018), are responsible for the incomplete knowledge of the active tectonics in that zone. Toward the South, thanks to specific works carried out after the 1995 Macas earthquake (Mw 7.1), the tectonics of the Cutucú uplift is better understood.

The subandean domain is dominated by reverse faulting (Rivadeneira and Baby, 2004). In northern Ecuador, the Napo uplift (zone 5) is considered to result from a sub-horizontal crustal decollement steepening close to the surface (Rivadeneira et al., 2004). Reverse FMs show variable fault plane azimuths (Fig. 10) which can be the expression of such type of structures. The strain rates are the lowest of the described zones, probably because most of the deformation is absorbed by the CCPP system and faults in the NAS. From the strain tensor, a dominant E-W shortening is expected for this area (Fig. 10).

The southeastern Cutucú seismic zone (zone 6) is the source of the 1995 Macas earthquake (Mw 7.0, GCMT); it is a complex system with almost parallel thrusts and decollements with a NNE trend (Bes de Berc, 2003). The complexity of the fault system could be an element explaining the diversity of the observed mechanisms (reverse and strike-slip, shown by both MECAVEL and GCMT solutions; see Fig. 8). However, we cannot exclude the possibility that some solutions (e.g. around latitude ~2°S and longitude ~77.6°W) are not accurately determined, due to the absence of stations east of the earthquakes. The strain rate is relatively low and shows shortening in a NW-SE direction (Fig. 10), which is consistent with the existence of the Cutucú Range and its NNE strike.

4.2.3. Western cordillera

The El Angel fault (zone 8) is the southernmost expression of NNE trending structures that are clearly recognizable along the western slopes of the Cordillera Central in Colombia, defined as the Romeral fault system (París et al., 2000). Geomorphic lineaments have right-lateral strike-slip motion (Ego et al., 1995). In 1868, a segment attributed to this system ruptured twice with Mic (magnitude based on intensity observations) of 6.6 and 7.2, respectively (Beauval et al., 2010). In the recent years analyzed here, seismicity concentrates close to the Cerro Negro-Chiles volcanic complex, where a magmatic intrusion likely started in the second semester of 2013 (Ebmeier et al., 2016). The main Mw 5.6 earthquake, studied using satellite radar data (Ebmeier et al., 2016), shows a predominantly right-lateral slip with a slight reverse component, in agreement with the MECAVEL solution. The other FMs also show right-lateral strike-slip motion and E-W shortening, but no comparison can be done here with a GPS-derived strain tensor, due to the insufficient GPS coverage of the area (Fig. S1).

The Quito and Latacunga seismic sources (zone 9) are composed by blind reverse faults, folds and flexures at the surface, delimiting a possible block separated from the NAS (Alvarado et al., 2016). The Quito portion (N–S direction and ~60 km long) is a five sub-segments structure, which can rupture individually or simultaneously with magnitudes from 5.7 to 7.1 (Alvarado et al., 2014). The FMs in this section show ~ N–S reverse planes which are consistent with the shortening predicted by the strain rates derived from GPS velocities. Along the Latacunga segment, we only have one solution with a N–S nodal plane indicating EW shortening, in agreement with the proposed kinematic model from Lavenu et al. (1995) and Alvarado et al. (2016).

4.3. Deep sources

The intermediate and deep seismicity is related to the subduction of Nazca and Farallon slabs (Fig. 12). The Nazca slab, however, only hosts a weak and low magnitude seismicity in Ecuador. We could solve for two intermediate-depth FMs (~100 km), in the area of La Mana (Fig. 12), which both show a combination of normal and strike-slip mechanisms. The small number of events prevents us to properly describe the rupture characteristics of this seismic source.

The Farallon seismic sources located south of the extension of the Grijalva margin (Loja, Morona, Loreto and Puyo in Fig. 12) exhibit recurrent seismicity along the slab, from shallow (~35 km) to intermediate depths (~250 km). We generally observe that at least one of the nodal planes has a strike following the slab contour. At relatively shallow depths (between 40 and 90 km), from the Peru border to the Guayaquil area, the seismicity is mostly strike-slip (Fig. 12). The deeper seismicity is dominated by normal events, in agreement with the old deep part of the Farallon plate generating strong slab-pull forces (e.g. Chen et al., 2004). A highly active seismicity cluster is related to the El Puyo seismic nest, which spans over a wide range of depths from 130 to 250 km. Higher magnitude earthquakes appear to occur in the deeper portion of the nest, at depths around 200 km, as illustrated by the Mw 7.1 earthquake of August 2010. Another less dense and active normal-faulting cluster is located in the southeastern part of our study zone (Fig. 12), and shallower events (~120–160 km deep) are observed there.

5. Conclusions

We provide here a new catalog of earthquake focal mechanisms in Ecuador, obtained by waveform modeling. Our catalog includes 282 reliable solutions of source parameters for the period 2009–2015. This information includes the nodal plane angles as well as depth and moment magnitude determinations. Together with the GCMT solutions, our results provide new constraints on the interpretation of the tectonic processes at work in Ecuador. Combined with GPS-derived strain rates, these solutions put a better control on the deformation to be expected along and around the CCPP (Cosanga-Chingual-Pallatanga-Puná) fault system, which delimits the eastern boundary of the North Andean Sliver. In particular, the strike-slip character of the Puná fault, predicted by GPS strain rates and which was not fully recognized by the large magnitude GCMT mechanisms, now appears more clearly. At the Ecuador subduction zone, the focal mechanisms reflect the interseismic coupling derived from GPS: thrust interface mechanisms characterize the coupled interface in Northern Ecuador, while the low-to-moderate coupling in Central and Southern Ecuador results in variable fault plane orientations. This suggests that in case of low locking at the subduction interface, the stress field within the surrounding medium is poorly controlled by the plate motion and rather reflects heterogeneous deformation within the slab or the overriding crust.

Acknowledgments

We are grateful to the Secretaría Nacional de Educación Superior, Ciencia y Tecnología (SENESCYT, Ecuador) for funding the PhD scholarship of the first author of this study. This work has been supported by the Institut de Recherche pour le Développement of France (IRD) and the Instituto Geofísico, Escuela Politécnica Nacional (IG-EPN), Quito, Ecuador in the frame of the Joint International Laboratory 'Earthquakes and Volcanoes in the Northern Andes' (grant IRD 303759/00). Fundings from the Agence Nationale de la Recherche of France (grant ANR-07-BLAN-0143-01), SENESCYT (grant Fortalecimiento del Instituto Geofísico), SENPLADES (grant Generación de Capacidades para la Difusión de Alertas Tempranas), and collaboration with Instituto Geográfico Militar (IGM) are acknowledged. We thank all these partners for their strong support to the projects of geophysical instrumentation in Ecuador (national seismic and geodetic networks, and local ADN and JUAN projects). The installation and maintenance of the seismic and geodetic arrays would not have been possible without the help of numerous colleagues from the IRD and IG-EPN. The data from the OTAV station (IU network, https://doi.org/10.7914/SN/IU), retrieved at the IRIS Data Management Center, were used in this study. Numerical computations were partly performed on the S-CAPAD platform, IPGP, France. Comments and encouraging exchange of ideas with M. Segovia have contributed to enrich this study. Important remarks made during the review process, in particular by one of the two anonymous reviewers, were very helpful for this study. We finally thank the Editor (F. Audemard) for his careful rereading of the manuscript.

Appendix A. Supplementary data

Supplementary data to this article can be found online at https://doi.org/10.1016/j.jsames.2019.05.017.

References

Aguilar, J., Chatelain, J.-L., Guillier, B., Yepes, H., 1996. The Pisayambo, Ecuador, seismicity nest: towards the birth of a volcano? In: Geodinámica Andina, Troisième symposium international sur la Géodynamique Andine, Collection Colloques et Séminaires. ORSTOM édition, Paris, pp. 126–129.

Aktug, B., Nocquet, J.-M., Cingöz, A., Parsons, B., Erkan, Y., England, P., 2009. Deformation of western Turkey from a combination of permanent and campaign GPS data: limits to block-like behavior. J. Geophys. Res. 114, B10404. https://doi.org/10.1029/2008JB006000.

Alvarado, A., Audin, L., Nocquet, J.-M., Lagreulet, S., Segovia, M., Font, Y., Lamarque, G., Yepes, H., Mothes, P., Rolandone, F., Jarrin, P., Quidelleur, X., 2014. Active tectonics in Quito, Ecuador, assessed by geomorphological studies, GPS data, and crustal seismicity. Tectonics 33, 67–83. https://doi.org/10.1002/2012TC003224.

Alvarado, A., Audin, L., Nocquet, J.-M., Jaillard, E., Mothes, P., Jarrin, P., Segovia, M., Rolandone, F., Cisneros, D., 2016. Partitioning of oblique convergence in the northern Andes subduction zone: migration history and present-day boundary of the North Andean sliver in Ecuador. Tectonics 35, 1048–1065. https://doi.org/10.1002/2016TC004117.

Alvarado, A., Ruiz, M., Mothes, P., Yepes, H., Segovia, M., Vaca, M., Ramos, C., Enríquez, W., Ponce, G., Jarrín, P., Aguilar, J., Acero, W., Vaca, S., Singaucho, J.C., Pacheco, D., Córdova, A., 2018. Seismic, volcanic, and geodetic networks in Ecuador: building capacity for monitoring and research. Seismol Res. Lett. 89, 432–439. https://doi.org/10.1785/0220170229.

Audemard, F.A., 1993. Néotectonique, sismotectonique et aléa sismique du Nord-ouest du Vénézuéla (système de failles d'Oca-Ancón). PhD thesis. Université Montpellier II, Montpellier, France.

Audemard, F.E., Audemard, F.A., 2002. Structure of the Mérida Andes, Venezuela: relations with the south America–caribbean geodynamic interaction. Tectonophysics 345 (1–4), 1–26.

Avouac, J.-P., Meng, L., Wei, S., Wang, T., Ampuero, J.-P., 2015. Lower edge of locked main Himalayan thrust unzipped by the 2015 Gorkha earthquake. Nat. Geosci. 8, 708–711. https://doi.org/10.1038/ngeo2518.

Baize, S., Audin, L., Winter, T., Alvarado, A., Pilatasig, L., Taipe, M., Reyes, P., Kauffman, P., Yepes, H., 2015. Paleoseismology and tectonic geomorphology of the Pallatanga fault (central Ecuador), a major structure of the South American crust. Geomorphology 237, 14–28. https://doi.org/10.1016/j.geomorph.2014.02.030.

Beauval, C., Yepes, H., Bakun, W., Egred, J., Alvarado, A., Singaucho, J.-C., 2010. Locations and magnitudes of historical earthquakes in the Sierra of Ecuador (1587-1996). Geophys. J. Int. 181, 1613–1633. https://doi.org/10.1111/j.1365-246X.2010.04569.x.

Beauval, C., Yepes, H., Palacios, P., Segovia, M., Alvarado, A., Font, Y., Aguilar, J., Troncoso, L., Vaca, S., 2013. An earthquake catalog for seismic hazard assessment in Ecuador. Bull. Seismol. Soc. Am. 103 (2A), 773–786. https://doi.org/10.1785/0120120270.

Beauval, C., Marinière, J., Yepes, H., Audin, L., Nocquet, J.-M., Alvarado, A., Baize, S., Aguilar, J., Singaucho, J.-C., Jomard, H., 2018. A new seismic hazard model for Ecuador. Bull. Seismol. Soc. Am. 108 (3A), 1443–1464. https://doi.org/10.1785/0120170259.

Beck, S., Ruff, L., 1984. The rupture process of the great 1979 Colombia earthquake: evidence for the asperity model. J. Geophys. Res. 89, 9281–9291. https://doi.org/10.1029/JB089iB11p09281.

Bes de Berc, S., 2003. Tectonique de chevauchement, surrection et incision fluviatile (Exemple de la zone Subandine Equatorienne, haut bassin Amazonien). Thèse de doctorat. Université Toulouse III – Paul Sabatier.

Béthoux, N., Segovia, M., Alvarez, V., Collot, J.-Y., Charvis, P., Gailler, A., Monfret, T., 2011. Seismological study of the central Ecuadorian margin: evidence of upper plate deformation. J. South Am. Earth Sci. 31, 139–152. https://doi.org/10.1016/j.jsames.2010.08.001.

Bishop, J.W., Lees, J.M., Ruiz, M.C., 2017. Receiver function stacks: initial steps for seismic imaging of Cotopaxi volcano, Ecuador. In: AGU Fall Meet, Abstr. 31.

Bonilla, L., Ruiz, M., Yepes, H., 1992. Evaluation of seismic hazard in Ecuador, Simposio

Internacional sobre Prevención de Desastres Sísmicos, Mem. UNAM, Mexico, pp. 118–125.
Bouchon, M., 1981. A simple method to calculate Green's functions for elastic layered media. Bull. Seismol. Soc. Am. 71 (4), 959–971.
Calahorrano, A., 2005. Structure de la marge du Golfe de Guayaquil (Equateur) et propriétés physiques du chenal de subduction à partir de données de sismique marine réflexion et réfraction. Thèse de Doctorat, Université Pierre et Marie Curie (Paris VI).
Chambat, F., 1996. Figure de la Terre : Gravimétrie, régime de contraintes et vibrations. Thèse de Doctorat. Université Paris, pp. 7.
Champenois, J., Baize, S., Vallée, M., Jomard, H., Alvarado, A., Espin, P., Ekström, G., Audin, L., 2017. Evidences of surface rupture associated with a low-magnitude (Mw 5.0) shallow earthquake in the Ecuadorian Andes. J. Geophys. Res. 122, 8446–8458. https://doi.org/10.1002/2017JB013928.
Chemenda, A., Lallemand, S., Bokun, A., 2000. Strain partitioning and interplate friction in oblique subduction zones: constraints provided by experimental modeling. J. Geophys. Res. 105 (B3), 5567–5581. https://doi.org/10.1029/1999JB900332.
Chen, P.-F., Bina, C.R., Okal, E.A., 2004. A global survey of stress orientations in subducting slabs as revealed by intermediate-depth earthquakes. Geophys. J. Int. 159 (2), 721–733. https://doi.org/10.1111/j.1365-246X.2004.02450.x.
Chlieh, M., Mothes, P., Nocquet, J.-M., Jarrin, P., Charvis, P., Cisneros, D., Font, Y., Collot, J.-Y., Villegas, J.-C., Rolandone, F., Vallée, M., Regnier, M., Segovia, M., Martin, X., Yepes, H., 2014. Distribution of discrete seismic asperities and aseismic slip along the Ecuadorian megathrust. Earth Planet. Sci. Lett. 400, 292–301. https://doi.org/10.1016/j.epsl.2014.05.027.
Collot, J.-Y., Michaud, F., Alvarado, A., Marcaillou, B., Sosson, M., Ratzov, G., Migeon, S., Calahorrano, A., Pazmiño, A., 2009. Visión general de la morfología submarina del margen convergente de Ecuador-Sur de Colombia: implicaciones sobre la transferencia de masa y la edad de la subducción de la Cordillera de Carnegie. Geología y Geofísica Marina y Terrestre. Ecuador. Spec. Pub. INOCAR-IRD. pp. 47–74.
Collot, J.-Y., Sanclemente, E., Nocquet, J.-M., Leprêtre, A., Ribodetti, A., Jarrin, P., Chlieh, M., Graindorge, D., Charvis, P., 2017. Subducted oceanic relief locks the shallow megathrust in central Ecuador. J. Geophys. Res. 122, 3286–3305. https://doi.org/10.1002/2016JB013849.
Delouis, B., 2014. FMNEAR: determination of focal mechanism and first estimate of rupture directivity using near-source records and a linear distribution of point sources. Bull. Seismol. Soc. Am. 104, 1479–1500. https://doi.org/10.1785/0120130151.
Deniaud, Y., Baby, P., Basile, C., Ordoñez, M., Montenegro, G., Mascle, G., 1999. Opening and tectonic and sedimentary evolution of the Gulf of Guayaquil: neogene and Quaternary fore-arc basin of the south Ecuadorian Andes. C. R. Acad. Sci. Paris 328, 181–187.
Dumont, J.-F., Santana, E., Vilema, W., Pedoja, K., Ordóñez, M., Cruz, M., Jiménez, N., Zambrano, I., 2005. Morphological and microtectonicanalysis of quaternary deformation from Puná and Santa Clara islands, gulf of Guayaquil, Ecuador (south America). Tectonophysics 399 (1–4), 331–350. https://doi.org/10.1016/j.tecto.2004.12.029.
Durand, P., Massinon, B., Menechal, Y., Troiville, C., 1987. Etude sismique du site de Mica-Tambo (Equateur), Commissariat à l'Energie Atomique. Laboratoire de Géophysique, Rapport No.1.
Dziewonski, A., Chou, T., Woodhouse, J., 1981. Determination of earthquake source parameters from waveform data for studies of global and regional seismicity. J. Geophys. Res. 86, 2825–2852. https://doi.org/10.1029/JB086iB04p02825.
Ebmeier, S., Elliott, J., Nocquet, J.-M., Biggs, J., Mothes, P., Jarrín, P., Yépez, M., Aguaiza, S., Lundgren, P., Samsonov, S., 2016. Shallow earthquake inhibits unrest near Chiles–Cerro Negro volcanoes, Ecuador–Colombian border. Earth Planet. Sci. Lett. 450, 283–291. https://doi.org/10.1016/j.epsl.2016.06.046.
Ego, F., Sébrier, M., Yepes, H., 1995. Is the Cauca-Patia and Romeral fault system left or right lateral? Geophys. Res. Lett. 22, 33–36. https://doi.org/10.1029/94GL02837.
Ego, F., Sébrier, M., Lavenu, A., Yepes, H., Egüez, A., 1996. Quaternary state of stress in the northern Andes and the restraining bend model for the Ecuadorian Andes. Tectonophysics 259 (1), 101–116. https://doi.org/10.1016/0040-1951(95)00075-5.
Egred, J., 2000. El Terremoto de Riobamba. Abya Yala, Quito.
Egüez, A., Alvarado, A., Yepes, H., Machette, M., Costa, C., Dart, R., 2003. Database and Map of Quaternary Faults and Folds of Ecuador and its Offshore Regions. U.S. Geol. Survey, pp. 1–77 Open File Report, 03-289.
Ekström, G., Nettles, M., Dziewonski, A., 2012. The global CMT project 2004–2010: centroid-moment tensors for 13,017 earthquakes. Phys. Earth Planet. In. 200 (201), 1–9. https://doi.org/10.1016/j.pepi.2012.04.002.
Font, Y., Segovia, M., Vaca, S., Theunissen, T., 2013. Seismicity pattern along the Ecuadorian subduction zone: new constraints from earthquake location in a 3D a priori velocity model. Geophys. J. Int. 193, 263–286. https://doi.org/10.1093/gji/ggs083.
Freymueller, J., Kellogg, J., Vega, V., 1993. Plate motions in the North andean region. J. Geophys. Res. 98, 21853–21863. https://doi.org/10.1029/93jb00520.
Grandin, R., Vallée, M., Lacassin, R., 2017. Rupture process of the Oklahoma Mw 5.7 Pawnee earthquake from Sentinel-1 InSAR and seismological data. Seismol Res. Lett. 88, 994–1004. https://doi.org/10.1785/0220160226.
Hall, M., 2000. Los terremotos del Ecuador del 5 de marzo de 1987 deslizamientos y sus efectos socioeconómicos, Colección de Estudios de Geografía, vol. 9 Corporación Editora Nacional, Quito, Ecuador.
Hayes, G., Wald, D., Johnson, R., 2012. Slab1.0: a three-dimensional model of global subduction zone geometries. J. Geophys. Res. 117, B01302. https://doi.org/10.1029/2011JB008524.
Jarrin, P., 2015. Modelamiento de datos GPS aplicado al estudio de la subducción en el Ecuador. Reporte de Master. Escuela Politécnica Nacional, Quito-Ecuador.
Kanamori, H., McNally, K., 1982. Variable rupture mode of the subduction zone along the Ecuador-Colombia coast. Bull. Seismol. Soc. Am. 72, 1241–1253.
Kawakatsu, H., Proaño, G., 1991. Focal mechanisms of the march 6, 1987 Ecuador earthquakes. J. Phys. Earth 39, 589–597. https://doi.org/10.4294/jpe1952.39.589.
Kelleher, J., 1972. Rupture zones of large South American earthquakes and some predictions. J. Geophys. Res. 77, 2087–2103. https://doi.org/10.1029/JB077i011p02087.
Kellogg, J., Bonini, W., 1982. Subduction of the Caribbean plate and basement, uplifts in the overriding south American plate. Tectonics 1 (3), 251–276. https://doi.org/10.1029/TC001i003p00251.
Kellogg, J., Ogujiofor, I., Kansaka, D., 1985. Cenozoic tectonics of the Panama and north Andes blocks. Memorias Congreso Latinoamericano de Geologia 6, 34–49.
Kendrick, E., Bevis, M., Smalley, R., Brooks, B., Vargas, R., Lauría, E., Fortes, L., 2003. The Nazca-South America Euler vector and its rate of change. J. South Am. Earth Sci. 16, 125–131. https://doi.org/10.1016/S0895-9811(03)00028-2.
Lavenu, A., Winter, T., Dávila, F., 1995. A pliocene-quaternary compressional basin in the Interandean Depression Central Ecuador. Geophys. J. Int. 121, 279–300. https://doi.org/10.1111/j.1365-246X.1995.tb03527.x.
Lonsdale, P., 2005. Creation of the cocos and Nazca plates by fission of the Farallon plate. Tectonophysics 404, 237–264. https://doi.org/10.1016/j.tecto.2005.05.011.
López, E., 2005. 132 años de historia del Observatorio Astronómico de Quito, Observatorio Astronómico Nacional. Escuela Politécnica Nacional.
Marshak, S., Nelson, W., McBride, J., 2003. Phanerozoic strike-slip faulting in the continental interior platform of the United States: examples from the Laramide Orogen, midcontinent, and Ancestral Rocky mountains. Geol. Soc. Spec. Publ. 210, 159–184. https://doi.org/10.1144/GSL.SP.2003.210.01.10.
McCaffrey, R., 1992. Oblique plate convergence, slip vectors, and forearc deformation. J. Geophys. Res. 97 (B6), 8905–8915. https://doi.org/10.1029/92JB00483.
McNutt, S., 2005. Volcano seismology. Annu. Rev. Earth Planet Sci. 33, 461–491.
Mendoza, C., Dewey, J., 1984. Seismicity associated with the great Colombia-Ecuador earthquakes of 1942, 1958, and 1979: implications for barrier models of earthquake rupture. Bull. Seismol. Soc. Am. 74 (2), 577–593.
Mercier de Lépinay, B., Deschamps, A., Klingelhoefer, F., Mazabraud, Y., Delouis, B., Clouard, V., Hello, Y., Crozon, J., Marcaillou, B., Graindorge, D., Vallée, M., Perrot, J., Bouin, M.-P., Saurel, J.-M., Charvis, P., St-Louis, M., 2011. The 2010 Haiti earthquake: a complex fault pattern constrained by seismologic and tectonic observations. Geophys. Res. Lett. 38, L22305. https://doi.org/10.1029/2011GL049799.
Michaud, F., Collot, J.-Y., Alvarado, A., López, E., the scientific and technical team of INOCAR, 2006. Batimetría Y Relieve Continental. publication IOA-CVM-02-Post, Inst. Oceanogr. de la Armada del Ecuador, Guayaquil.
Minson, S., Dreger, D., Burgmann, R., Kanamori, H., Larson, K., 2007. Seismically and geodetically determined nondouble-couple source mechanisms from the 2000 Miyakejima volcanic earthquake swarm. J. Geophys. Res. 112, 10308. https://doi.org/10.1029/2006JB004847.
Mora-Páez, H., Kellogg, J., Freymueller, J., Mencin, D., Fernandes, R., Diederix, H., LaFemina, P., Cardona-Piedrahita, L., Lizarazo, S., Peláez-Gaviria, J.-R., Díaz-Mila, F., Bohórquez-Orozco, O., Giraldo-Londoño, L., Corchuelo-Cuervo, Y., 2018. Crustal deformation in the northern Andes – a new GPS velocity field. J. South Am. Earth Sci. 89, 76–91. https://doi.org/10.1016/j.jsames.2018.11.002.
Mothes, P., Nocquet, J.-M., Jarrin, P., 2013. Continuous GPS network operating throughout Ecuador. Eos. Transactions AGU 94 (26), 229–231. https://doi.org/10.1002/2013EO260002.
Mothes, P., Rolandone, F., Nocquet, J.-M., Jarrin, P., Alvarado, A., Ruiz, M., Cisneros, D., Mora-Páez, H., Segovia, M., 2018. Monitoring the earthquake cycle in the northern Andes from the Ecuadorian cGPS network. Seismol Res. Lett. 89, 534–541. https://doi.org/10.1785/0220170243.
Nocquet, J.-M., Yepes, H., Vallée, M., Mothes, P., Regnier, M., Segovia, S., Font, Y., Vaca, S., Béthoux, N., Ramos, C., 2010. The ADN Project: an Integrated Seismic Monitoring of the Northern Ecuadorian Subduction. EGU General Assembly 2010, Vienna, Austria, pp. 9913.
Nocquet, J.-M., Villegas, J.-C., Chlieh, M., Mothes, P., Rolandone, F., Jarrin, P., Cisneros, D., Alvarado, A., Audin, L., Bondoux, F., Martin, X., Font, Y., Régnier, M., Vallée, M., Tran, T., Beauval, C., Maguiña, J., Martinez, W., Tavera, H., Yepes, H., 2014. Motion of continental slivers and creeping subduction in the northern Andes. Nat. Geosci. 7, 287–291. https://doi.org/10.1038/ngeo2099.
Nocquet, J.-M., Jarrin, P., Vallée, M., Mothes, P., Grandin, R., Rolandone, F., Delouis, B., Yepes, H., Font, Y., Fuentes, D., Régnier, M., Laurendeau, A., Cisneros, D., Hernandez, S., Sladen, A., Singaucho, J.-C., Mora, H., Gomez, J., Montes, L., Charvis, P., 2017. Supercycle at the Ecuadorian subduction zone revealed after the 2016 Pedernales earthquake. Nat. Geosci. 10, 145–149. https://doi.org/10.1038/NGEO2864.
París, G., Machette, M., Dart, R., Haller, K., 2000. Map and Database of Quaternary Faults and Folds in Colombia and its Offshore Regions. U.S. Geol. Survey Open File Report, 00-0284.
Pennington, W., 1981. Subduction of the eastern Panama basin and seismotectonics of northwestern south America. J. Geophys. Res. 86. https://doi.org/10.1029/JB086iB11p10753.
Poveda, E., Monsalve, G., Vargas, C., 2015. Receiver functions and crustal structure of the northwestern Andean region, Colombia. J. Geophys. Res. Solid Earth 120, 2408–2425. https://doi.org/10.1002/2014JB011304.
Rivadeneira, M., Baby, P., 2004. Características geológicas de los principales campos petroleros de Petroproducción, vol. 144 Travaux de l'Institut Français d'Etudes Andines.
Rivadeneira, M., Baby, P., Barragán, R., 2004. La Cuenca Oriente: geología y petróleo, vol. 144 Travaux de l'Institut Français d'Etudes Andines.
Robalino, F., 1977. Espesor de la corteza en Quito mediante el análisis del espectro de las ondas longitudinales P de período largo. Instituto Panamericano de Geografía e Historia, XI Asamblea General, Sección Nacional del Ecuador, Quito-Ecuador.

Rolandone, F., Nocquet, J.-M., Mothes, P.A., Jarrin, P., Vallée, M., Cubas, N., Hernandez, S., Plain, M., Vaca, S., Font, Y., 2018. Areas prone to slow slip events impede earthquake rupture propagation and promote afterslip. Sci. Adv. 4, eaao6596. https://doi.org/10.1126/sciadv.aao6596.

Sambridge, M., 1999. Geophysical inversion with a neighbourhood algorithm- I. Searching a parameter space. Geophys. J. Int. 138, 479–494. https://doi.org/10.1046/j.1365-246X.1999.00876.x.

Segovia, M., Alvarado, A., 2009. Breve análisis de la sismicidad y del campo de esfuerzos en el Ecuador, Geología y Geofísica Marina y Terrestre, Ecuador. Spec. Pub. INOCAR-IRD, pp. 131–149.

Segovia, M., Pacheco, J., Shapiro, N., Yepes, H., Guillier, B., Ruiz, M., Calahorrano, A., Andrade, D., Egred, J., 1999. The Agust 4, 1998, Bahía Earthquake (Mw = 7.1): Rupture Mechanism and Comments on the Potencial Seismic Activity. Fourth ISAG, Germany, pp. 673–677.

Segovia, M., 2016. Imagerie microsismique d'une asperité sismologique dans la zone de subduction Équatorienne. Thèse de doctorat. Université Nice-Sophia Antipolis.

Segovia, M., Font, Y., Régnier, M., Charvis, P., Galve, A., Nocquet, J.-M., et al., 2018. Seismicity distribution near a subducting seamount in the Central Ecuadorian subduction zone, space-time relation to a slow-slip event. Tectonics 37, 2106–2123. https://doi.org/10.1029/2017TC004771.

Shuler, A., Ekström, G., 2009. Anomalous earthquakes associated with Nyiragongo Volcano: observations and potential mechanisms. J. Volcanol. Geotherm. Res. 181, 219–230. https://doi.org/10.1016/j.jvolgeores.2009.01.011.

Soulas, J.-P., Egüez, A., Yepes, H., Pérez, V.-H., 1991. Tectónica activa y riesgo sísmico en los Andes Ecuatorianos y en el extremo Sur de Colombia. Bol. Geol. Ecuatoriano 2 (1), 3–11.

Swenson, J., Beck, S., 1996. Historical 1942 Ecuador and 1942 Peru subduction earthquakes and earthquake cycles along Colombia, Ecuador and Peru subduction segments. Pure Appl. Geophys. 146 (1), 67–101.

Taboada, C., Dimaté, C., Fuenzalida, A., 1998. Sismotectónica de Colombia: deformación continental activa y subducción. Física Tierra 10, 111–147.

Tibaldi, A., Rovida, A., Corazzato, C., 2007. Late Quaternary kinematics, slip-rate and segmentation of a major Cordillera-parallel transcurrent fault: the Cayambe-Afiladores-Sibundoy system, NW South America. J. Struct. Geol. 29 (4), 664–680. https://doi.org/10.1016/j.jsg.2006.11.008.

Trenkamp, R., Kellogg, J., Freymueller, J., Mora, H., 2002. Wide plate margin deformation, southern Central America and northwestern South America, CASA GPS observations. J. South Am. Earth Sci. 15, 157–171.

Troncoso, L., 2008. Estudio sismológico del nido de Pisayambo. Reporte de Master. Escuela Politécnica Nacional, Quito-Ecuador.

Vaca, S., 2006. Elaboración de un modelo 3D de velocidades sísmicas de ondas para el Ecuador y relocalización de eventos sísmicos entre 1995 y 2005, Tesis de ingeniería. Facultad de Geología, Escuela Politécnica Nacional, Quito-Ecuador, pp. 63–66.

Vaca, S., Régnier, M., Bethoux, N., Alvarez, V., Pontoise, B., 2009. Sismicidad de la región de Manta: Enjambre sísmico de Manta-2005, Geología y Geofísica Marina y Terrestre, Ecuador. Spec. Pub. INOCAR-IRD, pp. 155–166.

Vaca, S., Vallée, M., Nocquet, J.-M., Battaglia, J., Regnier, M., 2018. Recurrent Slow Slip Events as a barrier to the northward rupture propagation of the 2016 Pedernales earthquake (Central Ecuador). Tectonophysics 724–725, 80–92. https://doi.org/10.1016/j.tecto.2017.12.012.

Vaca, S., Vallée, M., Nocquet, J.-M., Alvarado, A., 2019. Seismic Source Parameters of the 282 Ecuador Earthquakes (2009-2015) Determined by the MECAVEL Method. Mendeley data.

Vallée, M., Nocquet, J.-M., Battaglia, J., Font, Y., Segovia, M., Régnier, M., Mothes, P., Jarrin, P., Cisneros, D., Vaca, S., Yepes, H., Martin, X., Béthoux, N., Chlieh, M., 2013. Intense interfece seismiscity triggered by a shallow slow slip event in the Central Ecuador subduction zone. J. Geophys. Res. 118, 1–17. https://doi.org/10.1002/jgrb.50216.

Villegas-Lanza, J.-C., Chlieh, M., Cavalié, O., Tavera, H., Baby, P., Chire-Chira, J., Nocquet, J.-M., 2016. Active tectonics of Peru: heterogeneous interseismic coupling along the Nazca megathrust, rigid motion of the Peruvian Sliver, and Subandean shortening accommodation. J. Geophys. Res. 121, 7371–7394. https://doi.org/10.1002/2016JB013080.

Winter, T., Avouac, J.-P., Lavenu, A., 1993. Late Quaternary kinematics of the Pallatanga strike-slip fault (Central Ecuador) from topographic measurements of displaced morphological features. Geophys. J. Int. 115, 905–920. https://doi.org/10.1111/j.1365-246X.1993.tb01500.x.

Witt, C., Bourgois, J., Michaud, F., Ordoñez, M., Jiménez, N., Sosson, M., 2006. Development of the gulf of Guayaquil (Ecuador) during the quaternary as an effect of the north andean block tectonic escape. Tectonics 25, TC3017. https://doi.org/10.1029/2004TC001723.

Ye, L., Kanamori, H., Avouac, J.-P., Li, L., Cheung, K., Lay, T., 2016. The 16 April 2016, Mw 7.8 (MS 7.5) Ecuador earthquake: a quasi-repeat of the 1942 MS 7.5 earthquake and partial re-rupture of the 1906 MS 8.6 Colombia–Ecuador earthquake. Earth Planet. Sci. Lett. 454, 248–258. https://doi.org/10.1016/j.epsl.2016.09.006.

Yepes, H., 1982. Estudio de la actividad microsísmica en el Valle Interandino entre las latitudes 0.00° y 1.00° S, Tesis Ing. Geólogo. Escuela Politécnica Nacional, Quito, pp. 1–98.

Yepes, H., Audin, L., Alvarado, A., Beauval, C., Aguilar, J., Font, Y., Cotton, F., 2016. A new view for the geodynamics of Ecuador: implication in seismogenic source definition and seismic hazard assessment. Tectonics 35, 1249–1279. https://doi.org/10.1002/2015TC003941.

Yoshimoto, M., Kumagai, H., Acero, W., Ponce, G., Vásconez, F., Arrais, S., Ruiz, M., Alvarado, A., Pedraza-García, P., Dionicio, V., Chamorro, O., Maeda, Y., Nakano, M., 2017. Depth-dependent rupture mode along the Ecuador-Colombia subduction zone. Geophys. Res. Lett. 44, 2203–2210. https://doi.org/10.1002/2016GL071929.

Zahradník, J., Janský, J., Plicka, V., 2008. Detailed waveform inversion for moment tensors of M ~ 4 events; examples from the Corinth Gulf, Greece. Bull. Seismol. Soc. Am. 98, 2756–2771. http://doi.org/10.1785/0120080124.